



Automatic Qubit Characterization and Gate Optimization with *QubiC*

YILUN XU, GANG HUANG, JAN BALEWSKI, ALEXIS MORVAN, KASRA NOWROUZI, and DAVID I. SANTIAGO, Lawrence Berkeley National Laboratory, USA
RAVI K. NAIK, BRAD MITCHELL, and IRFAN SIDDIQI, University of California at Berkeley, USA

As the size and complexity of a quantum computer increases, quantum bit (qubit) characterization and gate optimization become complex and time-consuming tasks. Current calibration techniques require complicated and verbose measurements to tune up qubits and gates, which cannot easily expand to the large-scale quantum systems. We develop a concise and automatic calibration protocol to characterize qubits and optimize gates using *QubiC*, which is an open source FPGA (field-programmable gate array)-based control and measurement system for superconducting quantum information processors. We propose multi-dimensional loss-based optimization of single-qubit gates and full XY-plane measurement method for the two-qubit CNOT gate calibration. We demonstrate the *QubiC* automatic calibration protocols are capable of delivering high-fidelity gates on the state-of-the-art transmon-type processor operating at the Advanced Quantum Testbed at Lawrence Berkeley National Laboratory. The single-qubit and two-qubit Clifford gate infidelities measured by randomized benchmarking are of $4.9(1.1) \times 10^{-4}$ and $1.4(3) \times 10^{-2}$, respectively.

CCS Concepts: • **Hardware** → **Quantum computation**; *Reconfigurable logic and FPGAs*; • **Computer systems organization** → *Real-time system architecture*; • **Software and its engineering** → **Development frameworks and environments**; • **Information systems** → **Computing platforms**;

Additional Key Words and Phrases: FPGA, gateware, quantum gate calibration, qubit control, NISQ, engineering software

ACM Reference format:

Yilun Xu, Gang Huang, Jan Balewski, Alexis Morvan, Kasra Nowrouzi, David I. Santiago, Ravi K. Naik, Brad Mitchell, and Irfan Siddiqi. 2022. Automatic Qubit Characterization and Gate Optimization with *QubiC*. *ACM Trans. Quantum Comput.* 4, 1, Article 3 (October 2022), 12 pages.

<https://doi.org/10.1145/3529397>

1 INTRODUCTION

Quantum computers, which harness and exploit the laws of quantum mechanics to process information, have the potential to revolutionize computation by making solvable certain types of classically intractable problems [1, 21]. In the near term **noisy intermediate-scale quantum**

This work was supported by the Advanced Scientific Computing Research Testbeds for Science program, by the High Energy Physics QUANTISED program, and by the Quantum Systems Accelerator under the Office of Science of the U.S. Department of Energy under Contract No. DE-AC02-05CH11231.

Authors' addresses: Y. Xu, G. Huang (corresponding author), J. Balewski, A. Morvan, K. Nowrouzi, and D. I. Santiago, Lawrence Berkeley National Laboratory, Berkeley, CA, 94720; emails: {yilunxu, ghuang, balewski, amorvan, knowrouzi, david.i.santiago}@lbl.gov; R. K. Naik, B. Mitchell, and I. Siddiqi, University of California at Berkeley, Berkeley, CA, 94720; emails: {rnaik24, bradmitchell, irfan_siddiqi}@berkeley.edu.

Publication rights licensed to ACM. ACM acknowledges that this contribution was authored or co-authored by an employee, contractor or affiliate of the United States government. As such, the Government retains a nonexclusive, royalty-free right to publish or reproduce this article, or to allow others to do so, for Government purposes only.

© 2022 Copyright held by the owner/author(s). Publication rights licensed to ACM.

2643-6817/2022/10-ART3 \$15.00

<https://doi.org/10.1145/3529397>

(NISQ) computing era, a lot of quantum algorithms have been developed on a broad range of applications [16, 27, 29]. Quantum algorithms are most commonly described by quantum circuits, which consist of quantum gates performed on one or more **quantum bits (qubits)**. The calibration of a quantum processor is the process of finding optimal control parameters to construct quantum gates to steer the evolution of quantum systems. Since many of the most severe errors emerge from imprecise calibration and system drift, qubit characterization and gate optimization are essential for successful quantum computations [8, 9].

Initial setup of a physical multi-qubit system is a complex procedure that involves multiple instruments and multiple optimizations [34, 35]. As the size and complexity of the quantum system increases, the manual qubit characterization and gate optimization will be a time-consuming and not extensible task. The physical qubit must be carefully calibrated routinely, because quantum information processors are sensitive to the environment [22] and the control hardware can have slow drift with time [5] to impact the gate fidelity. Existing calibration techniques [7, 19, 23, 24, 31, 32] are able to offer high-fidelity gates on state-of-the-art processors, with single-qubit and two-qubit gate infidelities below 1.0×10^{-3} and 1.5×10^{-2} , respectively. However, they require complicated and cumbersome measurements to tune up multiple parameters of each gate independently, which may take a long time, even hours. The calibration results of existing techniques can be accurate, but with the tradeoff that a large number of sequences are needed to gather the datasets, which cannot be expanded to the large-scale quantum systems easily. Therefore, a concise calibration protocol that has the possibility to be fully automated is a very desired feature for the multi-qubit system.

Here, we present an automatic qubit characterization and gate optimization method with *QubiC* (**Qubit Control**) system to tackle the calibration challenges and keep pace with rapidly evolving classical control requirements. *QubiC* system is an open source, **FPGA (field-programmable gate array)**-based, control and measurement system for superconducting quantum information processors [33, 36]. The system consists of electronics hardware, FPGA gateware, and engineering software. Leveraging the state-of-the-art FPGA technology, *QubiC* provides fully parametric waveform generation, analog response acquisition and manipulation and classical signal post-processing. *QubiC* allows researchers to control all levels of the software stack, which enables the execution of a broader class of computation experiments while also facilitating the implementation co-design at each level of the control stack in next generation systems.

2 SINGLE-QUBIT CHARACTERIZATION AND GATE OPTIMIZATION

The qubit bias point and the waveform of pulses driving gates on a qubit require per-qubit calibration. The calibration values depend on the various details of the chip manufacturing process, the readout and control circuitry, and in-fridge connectivity. Every qubit requires an initial detailed calibration, supplemented by a frequent re-calibration process. An arbitrary single-qubit U_3 -gate, parameterized by three arbitrary angles, can always be decomposed into a sequence of two rotations of the quantum state by 90 degrees along the X-axis and three virtual-Z gates with three arbitrary angles [15]. The virtual-Z gate is applied in software by injecting a specific phase offsets to the signal driving qubit oscillation and it does not require a calibration. Therefore, obtaining a high-fidelity X(90) gate¹ is the primary objective of the single-qubit calibration, allowing for an arbitrary U_3 -gate to be executed on this qubit.

We are focusing on superconducting transmon-type qubits [11], readout via coupling capacitance, and controlled by 5–6 GHz microwave pulses. The four initial calibration parameters, a.k.a. qubit bias, are: qubit frequency, readout resonator frequency, qubit drive amplitude, and readout

¹In the Bloch sphere representation, the X(90) and X(180) gates rotate qubit state around the X-axis by 90 and 180 degrees, respectively.

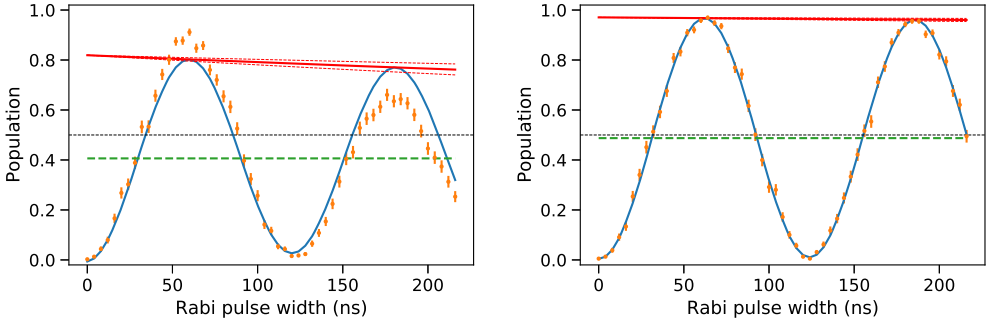


Fig. 1. Rabi oscillations induced on a qubit fitted with shape defined in Equation (1). Left: A crude initial calibration of the Rabi waveform results with a low amplitude, quickly decaying Rabi oscillations. The poor agreement of measured data (+) with the fitted shape (line) results with a large χ^2 . Right: The calibration from *autoRabi* optimizer yields much better signal. The maximal observed population is not reaching 1.0 because of the intrinsic hardware limitations. The readout correction has not been applied.

drive amplitude. A typical qubit driving pulse induces Rabi oscillations between the ground and the first excited state. The functional form of the Rabi oscillations is expected to follow the cosine shape with the amplitude decaying exponentially

$$P(t) = C + A \exp(-\tau t) \sin(2\pi f t + \phi_0), \quad (1)$$

where t is the length of the the Rabi waveform and C, A, τ, f, ϕ_0 parameters are fitted to the data.

QubiC contains the software and established procedures allowing for the initial calibration and re-calibration of the X(90) and X(180) gates.

The initial survey of the response of each qubit is done by sequentially exciting the resonator and, next, by inducing measurable Rabi oscillations of the qubit, as shown in Figure 1(a). The resonator readout amplitude is chosen based on linearity of the qubit response and is set at the possible high value to achieve good separation of the $|0\rangle$ and $|1\rangle$ states in the IQ-plane but not too high to avoid cross-talk between the qubits or populating the the second quantum state [25].

2.1 Automatic X(90) Gate Calibration

The qubit-resonator system responds to the qubit and the resonator driving pulses in a complex, non-linear fashion. Often, the three parameters—qubit frequency (f_q), Rabi drive amplitude (A_R), and readout frequency (f_r)—are optimized sequentially, which prevents adjustment of, say, f_r while optimizing for f_q , and so on.

We develop the *autoRabi* procedure, which aims to calibrate the X(90) gate by simultaneous adjustment of all three parameters. *autoRabi* minimizes the χ^2 -type loss function (\mathcal{L}_{tot}) over the vector of the unit-less quantities of concern ($\vec{\Delta}$)

$$\mathcal{L}_{tot} = \mathcal{L}_F + \mathcal{L}_{AC} + \mathcal{L}_T + \mathcal{L}_{BIC} \quad (2)$$

$$= \sum \Delta_i^2 \quad (3)$$

$$\vec{\Delta} = \left[\sqrt{\chi_{NDF}^2}, \frac{|A| - 0.5}{0.03}, \frac{C - 0.5}{0.05}, \frac{\frac{T_{X(90)}}{ns} - 32}{4.0}, \frac{\sigma(\delta_{BIC}(1))}{0.5}, \frac{\sigma(\delta_{BIC}(3))}{0.5}, \frac{\sigma(\delta_{BIC}(4))}{0.5} \right]. \quad (4)$$

The total loss \mathcal{L}_{tot} is composed of four unit-less terms:

- \mathcal{L}_F term assures the measured population matches the expected Rabi shape (Equation (1)). If the fit is poor, as in Figure 1(a), then the χ_{NDF}^2 term, being the reduced χ^2 , is large and dominates the loss.

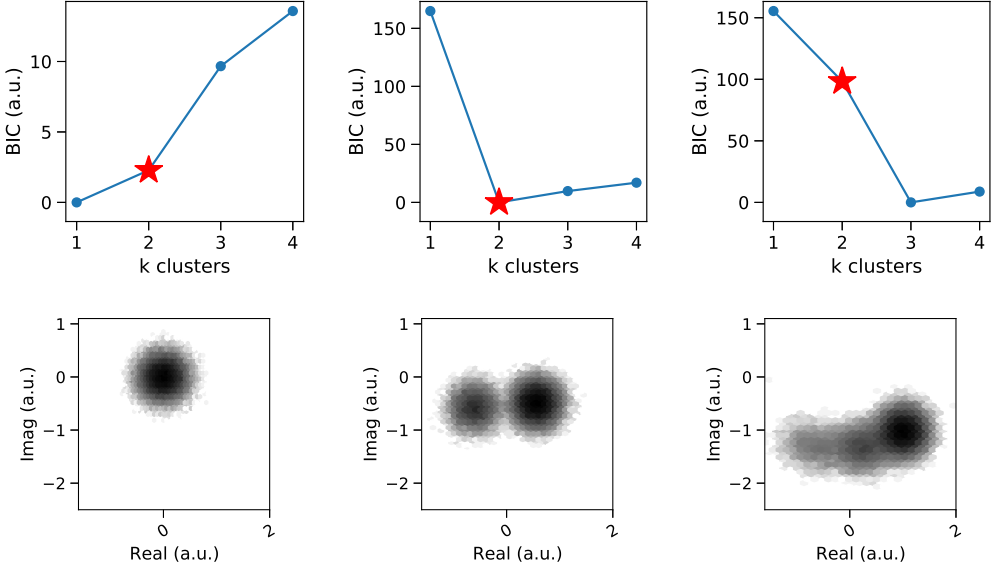


Fig. 2. Top: Bayesian Information Criterion BIC_k as function of assumed number of clusters (k) in the IQ-plane. Three columns correspond to three types of datasets with the true 1, 2, and 3 clusters, respectively. BIC has the minimum for the correct hypothesis of number of clusters. Bottom: raw IQ-pairs datasets used as inputs; the log of counts is represented by the gray scale.

- \mathcal{L}_{AC} expresses our preference for maximizing the Rabi amplitude (A) and the equal average population (C) of $|0\rangle$ and $|1\rangle$ states. The normalization constants of 0.03 and 0.05 are found empirically and are meant to reflect a subjective tradeoff between the goodness of the fit and the magnitude of the Rabi contrast.
- \mathcal{L}_T enforces the quantum state is rotated by 90 degrees by the Rabi waveform of the length of 32 ns^2 . The choice of normalization results with a 4 ns deviation of the Rabi period (equivalent to 360 degrees rotation) is as important as a change of the χ^2_{NDF} by 1 unit.
- \mathcal{L}_{BIC} ensures the hypothesis of the existence of 2-and-only-2 clusters in the IQ-plane is the most probable hypothesis. It is computed from **Bayesian Information Criterion (BIC)** [2].

The BIC_k is a criterion for model selection among a finite set of models; the model with the lowest BIC is the most likely. In our case, we vary the number of clusters (k), as shown in Figure 2 (top). Since the magnitude of BIC is very large and also depends on the sample size, a regularization is needed before it can be added to the total loss \mathcal{L}_{tot} in a robust fashion. We decided to combine the three BIC-based constraints

$$BIC_2 < BIC_k \text{ for } k \in [1, 3, 4] \quad (5)$$

using the sigmoid function $\sigma(\cdot)$ applied on the scaled difference of BICs

$$\sigma(x) = \frac{1}{1 + e^{-x}} \quad (6)$$

$$\delta_{BIC}(k) = (BIC_k - BIC_2)/10, \quad (7)$$

²Due to the *QubiC* hardware limitation, any waveform length must be a multiplicity of 4 ns, tied to the fixed frequency of the FPGA clock.

where the factor of 10 is chosen to attenuate the changes of BIC with k . Combining all the above leads to \mathcal{L}_{BIC} , which vanishes if all constraints in Equation (5) are met, otherwise \mathcal{L}_{BIC} never exceeds the four units of χ_{NDF}^2 to not overwhelm the \mathcal{L}_{tot} .

The coefficients weighting different contributions to \mathcal{L}_{tot} (see Equation (4)) have been chosen empirically. The underlying idea was to augment the first unweighted term being the reduced χ^2 from the Rabi oscillation fit with the constraints defining a good X(90) gate in a balanced way. Note, it may happen that a qubit drive frequency change commanded by the optimizer will be so large that the Rabi oscillations disappear. In such case the first term in Equation (4) becomes very large and it does not matter for the continuity of \mathcal{L}_{tot} that other terms may be undefined or non-computable. They can be dropped and the minimizer will recover.

To summarize, this definition of the total loss \mathcal{L}_{tot} simultaneously pushes the qubit bias point toward (i) fit to the Rabi spectrum is good ($\chi_{NDF}^2 \sim 1$), (ii) Rabi contrast is good ($A \sim C \sim 0.5$), (iii) the Rabi period is on target, (iv) the 2-and-only-2 clusters are most likely in the measured IQ-pairs distribution.

The *LMFIT* [18] package used already by *QubiC* offers over 20 minimization algorithms. For the *autoRabi* multi-dimensional optimization problem, we opted for a derivative free method. We have tried several optimization methods included in *LMFIT*, and the COBYLA minimizer [20]³ was performing very well.

Knowing theoretically predicted frequencies of qubits and readout resonators in a given chip, we can manually find an approximate initial qubit bias point at which recognizable Rabi oscillations are observed, as shown in Figure 1(a). This is the seed for COBYLA. We have bracketed the range of changes of the qubit and readout frequencies (f_q, f_r) at 2 MHz, and the Rabi drive amplitude change (A_R) at 0.3 of the full scale. For each iteration of COBYLA the following steps are executed:

- (1) COBYLA proposes a new set of values for: f_q, f_r, A_R ;
- (2) *QubiC* generates appropriate wave-forms, drives the qubit for the fixed number of shots, records and saves to discs the raw IQ-pairs;
- (3) Four GMM⁴ [6] fits are executed, assuming $k = [1..4]$ clusters, needed to collect $\delta_{BIC}(k)$ information;
- (4) GMM($k = 2$) is used to digitize the IQ-pairs into 0 or 1 bits and the probability of the $|1\rangle$ state is computed as a function of the length of the Rabi waveform;
- (5) Rabi oscillation parameters (A, C) and the χ_{NDF}^2 are extracted from the fit to the measured data;
- (6) value of loss \mathcal{L}_{tot} is computed based on Equation (2) and fed back to the next iteration of COBYLA.

Typically, *autoRabi* converges in about half an hour, after 40 iterations, each requiring *QubiC* to take 400 shots for 50 widths of the Rabi waveform. A typical improvement in the Rabi contrast is illustrated in Figure 1(b).

The *autoRabi* convergence time is dominated by the sum of time needed to drive, measure, and reset the qubit, rather than by classical computation required for post-processing and optimization performed by some particular choice of the CPU-FPGA hardware. The number of measurements (a.k.a. shots) required to achieve a certain statistical procession depends on the achievable purity of measured $|0\rangle, |1\rangle$ states. The length of each measurement is dominated by the qubit reset time. The third factor is non-linear change of response of the qubit, which may also slow down convergence of the minimizer and require more iterations.

³Constrained Optimization By Linear Approximation.

⁴Gaussian Mixture Model.

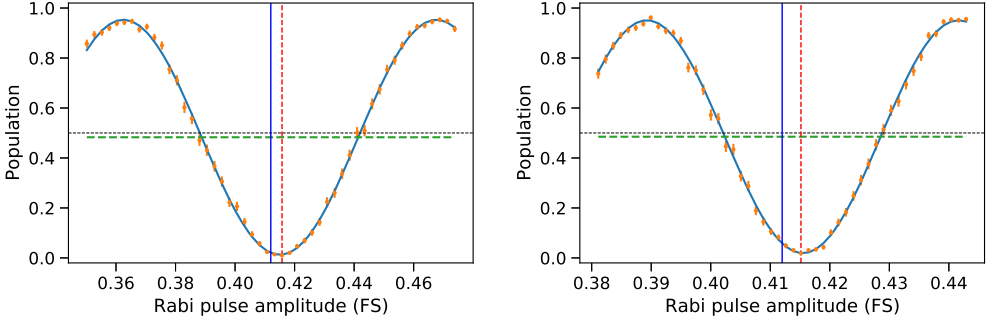


Fig. 3. Stacking of 16 X(90) gates (left) and 16 X(180) gates (right) applied on the 0-state qubit is equivalent to an identity-gate and allows for the fine-tuning of the waveform amplitude. The blue (solid) line is the initial value from *autoRabi*, the red (dashed) line is the optimal amplitude.

2.2 Fine-tuning of X(90) and X(180) Gates

The f_q , f_r , A_R values found by the *autoRabi* define the X(90) gate with a precision of 1–2 degrees of the state rotation. To achieve a better accuracy, we stack large numbers of the same gate and adjust the amplitude A_R , while keeping the duration of the gate constant. We prepare the initial qubit state to be $|0\rangle$ and stack the X(90) gate $N \times 4$ times to achieve a nominal identity gate. We sweep the A_R values in the vicinity of the value from *autoRabi* and fit the measured population probability with the sin-function. The optimal gate amplitude is found as the *arg minimum* of the fit, shown as vertical red (dashed) line in Figure 3(a). The optimal amplitudes for X(90) and X(180) differ a little because of the difference in the ratio of the length of the rising edge to the gate duration.

The envelopes of X(90) and X(180) gates implemented by *QubiC* include the DRAG term [17] as a default. The magnitude of the DRAG term is experimentally adjusted for every qubit and typically is stable over time. For that reason, DRAG adjustment is not included in the automatic calibration procedure.

The single-gate calibration procedures discussed in this section can be performed using *QubiC* software stack and allow for implementation of an arbitrary U_3 -gate. *QubiC* software also contains tools to calibrate the DRAG corrections, fine-tune the qubit drive frequency with T_2 Ramsey measurement, as well as measure T_1 and T_2 spin-echo.

The ultimate test of the fidelity of quantum gates is provided by the randomized benchmarking protocol and is discussed in the following Section 4.

3 TWO-QUBIT GATE (CNOT) CALIBRATION

3.1 Full Entanglement of Cross Resonance

Cross resonance (CR) is one of the methods to realize the two-qubit entanglement gate for the superconducting fixed-frequency transmon qubits [26]. We optimize the CR pulse of the cosine edge envelope with fixed ramp length to achieve maximal entanglement on the control and target qubits. To tune up a CR gate, we prepare the initial states of both qubits to be $|0\rangle$ and then apply the CR gate, followed by the target qubit state projection onto X, Y, and Z axis. The same process is repeated for the control qubit in $|1\rangle$. We fix the CR pulse length and sweep the CR pulse amplitude, resulting with six independent measurements that are combined into one value: the Bloch vector length $|\vec{R}|$ of the target qubit:

$$|\vec{R}| = \frac{1}{2} \sqrt{(X_0 - X_1)^2 + (Y_0 - Y_1)^2 + (Z_0 - Z_1)^2}, \quad (8)$$

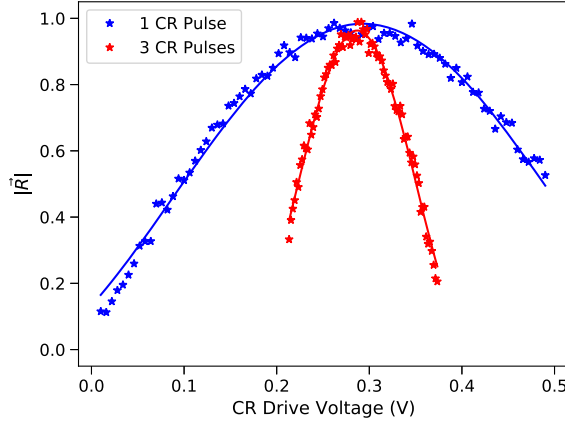


Fig. 4. CR measurement to search for the full entanglement. One and three CR pulses are employed for coarse and fine identification, respectively. The optimal value is found as *arg maximum* of the parabola fit.

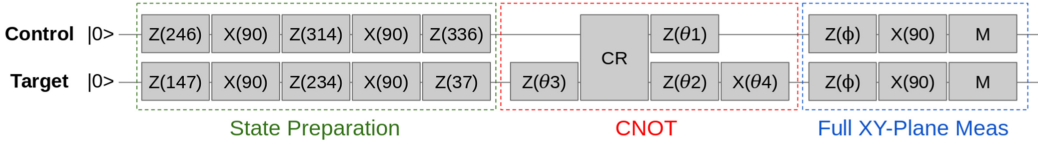


Fig. 5. Full XY-plane measurement schematic. Circuits are operated on the control qubit line and the target qubit line. The gate rotation angle is in the unit of degrees. M represents a measurement.

where X, Y, Z are the expectation values of the corresponding components of the target qubit, while the subscript 0, 1 are preparation states of the control qubit. The goal of the CR pulse amplitude sweeping is to achieve the full entanglement, where $|\vec{R}|$ is maximized. We can stack multiple CR pulses to make the $|\vec{R}|$ curve sharper to find the maximum more accurately. As shown in Figure 4, we implement one CR pulse for coarse identification and stacked three CR pulses for precise determination in the real measurement.

The CR echo sequence has been studied recently in References [4, 28], which could suppress the unwanted gate parameters and further improve the two-qubit gate fidelity. For simplicity, we only focus on the standard single-CR pulse in this section.

3.2 Full XY-plane Measurement and Fitting of CNOT

The CR pulse of particular length and amplitude can set two qubits in the fully entangled state, but typically additional single-qubit rotations are induced on each of the participating qubits. We need to attach a set of appropriate single-qubit gates before and after the CR pulse to obtain the real CNOT gate. It is common practice to project the qubit state to X/Y/Z axis for diagnosis. This is enough to evaluate if the state is good or not, but it would be good to gather more information about the state to help the optimization. Here, we develop a method called full XY-plane measurement, which projects both qubits states onto the measurement axis at the same angle in the XY-plane, sweeps the angle, and extracts the CNOT parameters from the curve fitting.

As shown in Figure 5, first, we need to prepare states for both control and target qubits. In general, the qubit state can be randomly chosen, as long as it is not sitting at the south pole or north pole on the Bloch sphere. A CNOT gate with zero initial values is employed after the state preparation. We then apply a virtual $Z(\phi)$ gate on a degenerate prepared state for both the control and target qubits, followed by an $X(90)$ gate for rotation, and we measure. Scanning the Z phase

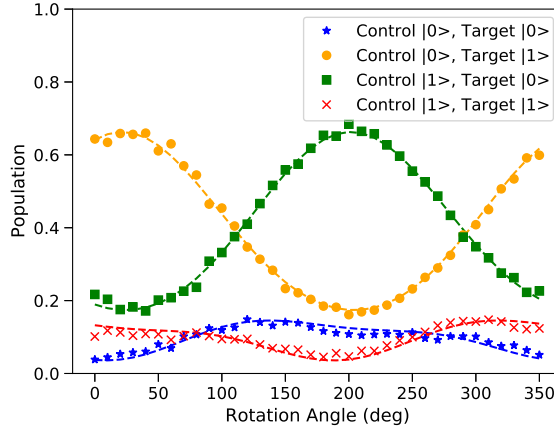


Fig. 6. Full XY-plane measurement (star points) and fitting (dashed lines) results. Four different colors represent four basis states $|00\rangle$, $|01\rangle$, $|10\rangle$, $|11\rangle$ of control and target qubits. We can see four unique patterns as a function of rotation angle ϕ among the four basis states, which can be distinguished by curve fitting. Each data point is an average of $\sim 2,000$ shots. The full XY-plane measurement and fitting only take ~ 1.5 minutes.

(ϕ) will project both states to any angle on the XY-plane. By scanning over the full XY-plane, we spread the noise among different angles, enabling us to extract the CNOT parameters from curve fitting by only executing one set of measurement, as shown in Figure 6.

We assume the CNOT gate relates to CR gate as follows:

$$CNOT = IX(\theta_4) \cdot ZZ(\theta_1, \theta_2) \cdot CR \cdot IZ(\theta_3), \quad (9)$$

where the CR represents the unitary for the CR pulse. If we describe the IX, ZZ, and IZ terms in the matrix form, then we will have

$$IX(\theta_4) = I \otimes R_X(\theta_4) = \begin{pmatrix} 1 & 0 \\ 0 & 1 \end{pmatrix} \otimes \begin{pmatrix} \cos \frac{\theta_4}{2} & -i \sin \frac{\theta_4}{2} \\ i \sin \frac{\theta_4}{2} & \cos \frac{\theta_4}{2} \end{pmatrix}, \quad (10)$$

$$ZZ(\theta_1, \theta_2) = R_Z(\theta_1) \otimes R_Z(\theta_2) = \begin{pmatrix} e^{-i \frac{\theta_1}{2}} & 0 \\ 0 & e^{i \frac{\theta_1}{2}} \end{pmatrix} \otimes \begin{pmatrix} e^{-i \frac{\theta_2}{2}} & 0 \\ 0 & e^{i \frac{\theta_2}{2}} \end{pmatrix}, \quad (11)$$

$$IZ(\theta_3) = I \otimes R_Z(\theta_3) = \begin{pmatrix} 1 & 0 \\ 0 & 1 \end{pmatrix} \otimes \begin{pmatrix} e^{-i \frac{\theta_3}{2}} & 0 \\ 0 & e^{i \frac{\theta_3}{2}} \end{pmatrix}, \quad (12)$$

where θ_1 , θ_2 , θ_3 , and θ_4 , are ZI phase, IZ phase, ZX phase, and IX phase, respectively. These four single-qubit parameters around the CR pulse need to be calculated from the curve fitting. R_X , R_Z represent the single-qubit rotation about the X, Z axis, while I is the identity gate. The symbol \otimes denotes the tensor product between two single-qubit rotation matrices. Since the CR pulse starting phase is not accumulated in the phase calculation, we add a constraint $\theta_2 + \theta_3 = 2\pi$ to use θ_2 to cancel out θ_3 .

Now, we take the inverse step of measurement schematic, adjusting the θ_1 , θ_2 , θ_3 , θ_4 to find the curve to match the measurement as shown in Figure 7. In the real measurement, we start with all the parameters (θ_1 , θ_2 , θ_3 , θ_4) equal to 0, as if the CR is a CNOT. The fitting of the parameters will tell us how far away the CR is from the real CNOT. If we describe the CR matrix as

$$CR = ZZ(\theta_1^F, \theta_2^F) \cdot IX(\theta_4^F) \cdot CNOT \cdot IZ(\theta_3^F), \quad (13)$$

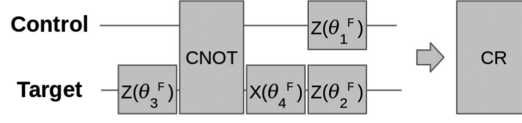


Fig. 7. Full XY-plane fitting schematic.

Table 1. Gate Infidelities and Errors

Gate	Gate Infidelity [†]	Process Infidelity	Unitary Error	Stochastic Error
Single-qubit Clifford	$4.9(1.1) \times 10^{-4}$	$1.3(1) \times 10^{-3}$	$1.9(9) \times 10^{-4}$	$1.2(1) \times 10^{-3}$
Two-qubit Clifford	$1.4(3) \times 10^{-2}$	$3.5(2) \times 10^{-2}$	$1.7(2) \times 10^{-2}$	$1.7(1) \times 10^{-2}$

[†]The gate infidelity was calculated as $\frac{3}{4}(1 - \frac{p_{\text{IRB}}}{p_{\text{SRB}}})$, where p_{IRB} and p_{SRB} are IRB and SRB decay parameters of Ap^m curves [14].

then the CNOT matrix can be derived as

$$\text{CNOT} = IX^{-1}(\theta_4^F) \cdot ZZ^{-1}(\theta_1^F, \theta_2^F) \cdot CR \cdot IZ^{-1}(\theta_3^F) = IX(-\theta_4^F) \cdot ZZ(-\theta_1^F, -\theta_2^F) \cdot CR \cdot IZ(-\theta_3^F), \quad (14)$$

where the superscript F represents the fitting parameters. The negative sign before the fitting parameters means that the final θ parameter will be the difference between the initial value and the fitted value, that is, $\theta = \theta_{\text{init}} - \theta_{\text{fit}}$. As shown in Figure 6, the measurement result agrees well with the matrix calculation, so the CNOT parameters can be extracted from the curve fitting by only implementing one set of measurement. It is noted that the full XY-plane measurement method will yield two sets of parameters for the CNOT gate, with a global phase of $\pi/2$ between them:

$$\text{CNOT} = IX(\theta_4) \cdot ZZ(\theta_1, \theta_2) \cdot CR \cdot IZ(\theta_3), \quad (15)$$

$$e^{i\frac{\pi}{2}} \text{CNOT} = IX(-\theta_4) \cdot ZZ(\theta_1 - \pi, \theta_2 - \pi) \cdot CR \cdot IZ(\theta_3 + \pi). \quad (16)$$

4 VALIDATION BY RANDOMIZED BENCHMARKING

To validate the performance of the automatic qubit characterization and gate optimization protocol, we implement **randomized benchmarking (RB)** [10] sequences on an 8-qubit quantum information processor [12] at the **Advanced Quantum Testbed (AQT)** in **Lawrence Berkeley National Laboratory (LBNL)** and evaluated the single-qubit and two-qubit gate fidelities. The **streamlined randomized benchmarking (SRB)** [13] is the standard protocol to characterize the probability of an error occurring during a gate, while the **interleaved randomized benchmarking (IRB)** [14] enhances SRB by estimating the average gate fidelity of specific gates. The **extended randomized benchmarking (XRB)** [30] enables us to distinguish unitary errors from stochastic errors in combination with SRB. As an illustration, the single-qubit X(90) and two-qubit CNOT gates are optimized using *QubiC* automatic calibration protocol and evaluated by SRB, IRB, and XRB, as shown in Figure 8. Table 1 illustrates the single-qubit and two-qubit Clifford gate infidelities and errors, which demonstrate that the automatic calibration protocol has the capability to deliver high-fidelity gates on state-of-the-art processors.

5 CONCLUSION

We develop an efficient and systematic method to automatically characterize qubits and optimize gates with *QubiC*, which is a customized FPGA-based Qubit Control system at LBNL. For the single-qubit calibration, the multi-dimensional loss-based optimization is proposed to characterize each

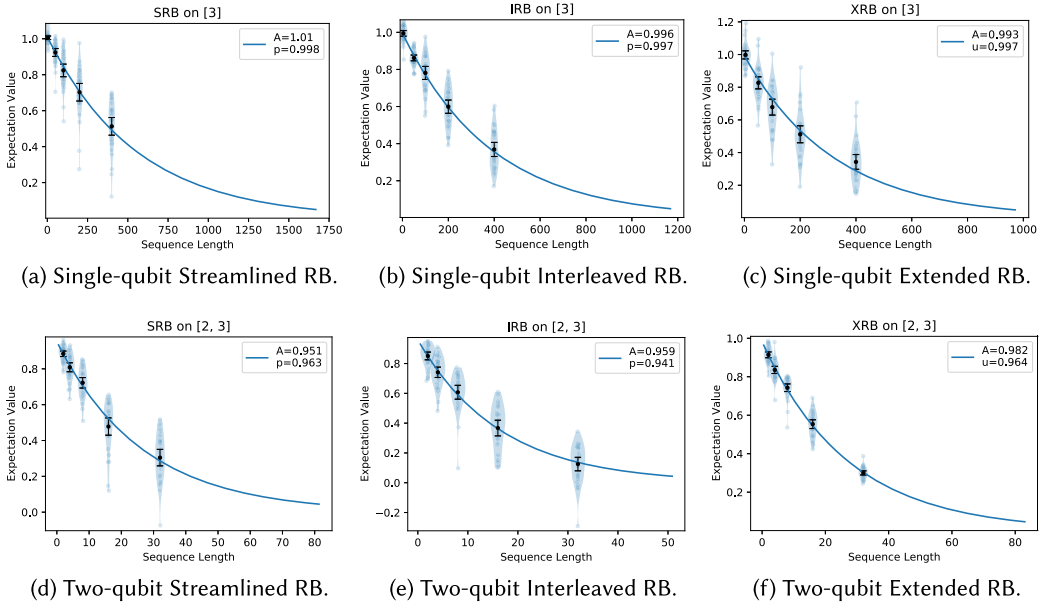


Fig. 8. RB results. We perform three kinds of RB protocols (SRB, IRB, XRB) on single qubit (Q3) and two qubits (Q2 and Q3), respectively. In each plot, each point corresponds to a measurement result of a random quantum circuit. The SRB and IRB curves are fitted with an exponential decay function Ap^m , while XRB curve is fitted with the function of Au^m , where p or u is the decay parameter. A is a constant that encapsulates the common state preparation and readout errors. The sequence length m is expressed in terms of Clifford gates. The RB data collected with *QubiC* are passed to the True-Q software [3] to fit the data and extract the parameters.

qubit on the quantum processor. With the stacking of consecutive identical gates, the drive amplitude is optimized to finely tune the single-qubit gate. For the two-qubit CNOT gate calibration, we stack multiple CR pulses and sweep CR pulse amplitude to achieve the full entanglement of the two qubits. We propose a full XY-plane measurement to project the qubit state to any angle on the XY-plane and extract the CNOT parameters from curve fitting by only implementing one set of measurements. The automatic qubit characterization and gate optimization protocols are validated by performing RB sequences on a superconducting quantum information processor. The measurement results demonstrate our method is capable of delivering high-fidelity gates on state-of-the-art processors.

To expand the method to large-scale quantum systems, we will adopt the qubit fast reset protocol in the calibration sequence to accelerate the process and automate the searching for initial qubit bias points. Regarding the two-qubit gate calibration, the **controlled phase (CZ)** gate and the echoed CR gate are potential candidates to further enhance the gate fidelity.

REFERENCES

- [1] Frank Arute, Kunal Arya, Ryan Babbush, Dave Bacon, Joseph C. Bardin, Rami Barends, Rupak Biswas, Sergio Boixo, Fernando G. S. L. Brandao, David A. Buell, et al. 2019. Quantum supremacy using a programmable superconducting processor. *Nature* 574, 7779 (2019), 505–510.
- [2] Bayesian information criterion. 2021. Wikipedia, the Free Encyclopedia. Retrieved from https://en.wikipedia.org/wiki/Bayesian_information_criterion.
- [3] Stefanie J. Beale, Arnaud Carignan-Dugas, Dar Dahlen, Joseph Emerson, Ian Hincks, Pavithran Iyer, Aditya Jain, David Hufnagel, Egor Ospadov, Jordan Saunders, Andrew Stasiuk, Joel J. Wallman, and Adam Winick. 2020. True-Q. (June 2020). DOI: <https://doi.org/10.5281/zenodo.3945250>

- [4] Antonio D. Córcoles, Jay M. Gambetta, Jerry M. Chow, John A. Smolin, Matthew Ware, Joel Strand, Britton L. T. Plourde, and Matthias Steffen. 2013. Process verification of two-qubit quantum gates by randomized benchmarking. *Phys. Rev. A* 87, 3 (2013), 030301.
- [5] Antonio D. Córcoles, Abhinav Kandala, Ali Javadi-Abhari, Douglas T. McClure, Andrew W. Cross, Kristan Temme, Paul D. Nation, Matthias Steffen, and Jay M. Gambetta. 2019. Challenges and opportunities of near-term quantum computing systems. *arXiv preprint arXiv:1910.02894* (2019).
- [6] Gaussian mixture model. 2021. Wikipedia, the Free Encyclopedia. Retrieved from https://en.wikipedia.org/wiki/Mixture_model#Gaussian_mixture_model.
- [7] IBM Quantum. 2021. Retrieved from <https://quantum-computing.ibm.com/>.
- [8] Julian Kelly, Peter O'Malley, Matthew Neeley, Hartmut Neven, and John M. Martinis. 2018. Physical qubit calibration on a directed acyclic graph. *arXiv preprint arXiv:1803.03226* (2018).
- [9] Paul V. Klimov, Julian Kelly, John M. Martinis, and Hartmut Neven. 2020. The snake optimizer for learning quantum processor control parameters. *arXiv preprint arXiv:2006.04594* (2020).
- [10] Emanuel Knill, Dietrich Leibfried, Rolf Reichle, Joe Britton, R. Brad Blakestad, John D. Jost, Chris Langer, Roee Ozeri, Signe Seidelin, and David J. Wineland. 2008. Randomized benchmarking of quantum gates. *Phys. Rev. A* 77, 1 (2008), 012307.
- [11] Jens Koch, Terri M. Yu, Jay Gambetta, A. A. Houck, D. I. Schuster, J. Majer, Alexandre Blais, M. H. Devoret, S. M. Girvin, and R. J. Schoelkopf. 2007. Charge-insensitive qubit design derived from the Cooper pair box. *Phys. Rev. A* 76, 4 (Oct. 2007), 042319.
- [12] J. M. Kreikebaum, K. P. O'Brien, A. Morvan, and I. Siddiqi. 2020. Improving wafer-scale Josephson junction resistance variation in superconducting quantum coherent circuits. *Superconduct. Sci. Technol.* 33, 6 (2020), 06LT02.
- [13] Easwar Magesan, Jay M. Gambetta, and Joseph Emerson. 2011. Scalable and robust randomized benchmarking of quantum processes. *Phys. Rev. Lett.* 106, 18 (2011), 180504.
- [14] Easwar Magesan, Jay M. Gambetta, Blake R. Johnson, Colm A. Ryan, Jerry M. Chow, Seth T. Merkel, Marcus P. Da Silva, George A. Keefe, Mary B. Rothwell, Thomas A. Ohki, et al. 2012. Efficient measurement of quantum gate error by interleaved randomized benchmarking. *Phys. Rev. Lett.* 109, 8 (2012), 080505.
- [15] David C. McKay, Christopher J. Wood, Sarah Sheldon, Jerry M. Chow, and Jay M. Gambetta. 2017. Efficient Z gates for quantum computing. *Phys. Rev. A* 96, 2 (Aug. 2017), 022330.
- [16] Ashley Montanaro. 2016. Quantum algorithms: An overview. *npj Quant. Inf.* 2, 1 (2016), 1–8.
- [17] Felix Motzoi, Jay M. Gambetta, Patrick Rebentrost, and Frank K. Wilhelm. 2009. Simple pulses for elimination of leakage in weakly nonlinear qubits. *Phys. Rev. Lett.* 103, 11 (2009), 110501.
- [18] Matthew Newville, Till Stensitzki, Daniel B. Allen, and Antonino Ingargiola. 2014. LMFIT: Non-Linear Least-Square Minimization and Curve-fitting for Python. (Sept. 2014). DOI: <https://doi.org/10.5281/zenodo.11813>
- [19] A. D. Patterson, J. Rahamim, T. Tsunoda, P. A. Spring, S. Jebari, K. Ratter, M. Mergenthaler, G. Tancredi, B. Vlastakis, M. Esposito, et al. 2019. Calibration of a cross-resonance two-qubit gate between directly coupled transmons. *Phys. Rev. Appl.* 12, 6 (2019), 064013.
- [20] M. J. D. Powell. 1998. Direct search algorithms for optimization calculations. *Acta Numer.* 7 (1998), 287–336.
- [21] John Preskill. 2018. Quantum computing in the NISQ era and beyond. *Quantum* 2 (2018), 79.
- [22] Timothy Proctor, Melissa Revelle, Erik Nielsen, Kenneth Rudinger, Daniel Lobser, Peter Maunz, Robin Blume-Kohout, and Kevin Young. 2020. Detecting and tracking drift in quantum information processors. *Nat. Commun.* 11, 1 (2020), 1–9.
- [23] M. A. Rol, C. C. Bultink, T. E. O'Brien, S. R. De Jong, L. S. Theis, Xiang Fu, F. Luthi, R. F. L. Vermeulen, J. C. de Sterke, Alessandro Bruno, et al. 2017. Restless tuneup of high-fidelity qubit gates. *Phys. Rev. Appl.* 7, 4 (2017), 041001.
- [24] Kenneth Rudinger, Shelby Kimmel, Daniel Lobser, and Peter Maunz. 2017. Experimental demonstration of a cheap and accurate phase estimation. *Phys. Rev. Lett.* 118, 19 (2017), 190502.
- [25] Daniel Sank, Zijun Chen, Mostafa Khezri, J. Kelly, R. Barends, B. Campbell, Y. Chen, B. Chiaro, A. Dunsworth, A. Fowler, et al. 2016. Measurement-induced state transitions in a superconducting qubit: Beyond the rotating wave approximation. *Phys. Rev. Lett.* 117, 19 (Nov. 2016).
- [26] Sarah Sheldon, Easwar Magesan, Jerry M. Chow, and Jay M. Gambetta. 2016. Procedure for systematically tuning up cross-talk in the cross-resonance gate. *Phys. Rev. A* 93, 6 (2016), 060302.
- [27] Adrien Suau, Gabriel Staffelbach, and Henri Calandra. 2021. Practical quantum computing: Solving the wave equation using a quantum approach. *ACM Trans. Quant. Comput.* 2, 1 (2021), 1–35.
- [28] Neereja Sundaresan, Isaac Lauer, Emily Pritchett, Easwar Magesan, Petar Jurcevic, and Jay M. Gambetta. 2020. Reducing unitary and spectator errors in cross resonance with optimized rotary echoes. *PRX Quant.* 1, 2 (2020), 020318.
- [29] Hayato Ushijima-Mwesigwa, Ruslan Shaydulin, Christian F. A. Negre, Susan M. Mniszewski, Yuri Alexeev, and Ilya Safro. 2021. Multilevel combinatorial optimization across quantum architectures. *ACM Trans. Quant. Comput.* 2, 1 (2021), 1–29.

- [30] Joel Wallman, Chris Granade, Robin Harper, and Steven T. Flammia. 2015. Estimating the coherence of noise. *New J. Phys.* 17, 11 (2015), 113020.
- [31] Gregory A. L. White, Charles D. Hill, and Lloyd C. L. Hollenberg. 2021. Performance optimization for drift-robust fidelity improvement of two-qubit gates. *Phys. Rev. Appl.* 15, 1 (2021), 014023.
- [32] Nicolas Wittler, Federico Roy, Kevin Pack, Max Werninghaus, Anurag Saha Roy, Daniel J. Egger, Stefan Filipp, Frank K. Wilhelm, and Shai Machnes. 2021. Integrated tool set for control, calibration, and characterization of quantum devices applied to superconducting qubits. *Phys. Rev. Appl.* 15, 3 (2021), 034080.
- [33] Yilun Xu, Gang Huang, Jan Balewski, Ravi Naik, Alexis Morvan, Bradley Mitchell, Kasra Nowrouzi, David I. Santiago, and Irfan Siddiqi. 2021. QubiC: An open-source FPGA-based control and measurement system for superconducting quantum information processors. *IEEE Trans. Quant. Eng.* 2 (2021), 1–11.
- [34] Yilun Xu, Gang Huang, Ravi Naik, Bradley Mitchell, David Santiago, and Irfan Siddiqi. 2020. Automatic single qubit characterization with QubiC. *Bull. Amer. Phys. Societ.* 65 (2020).
- [35] Yilun Xu, Gang Huang, Ravi Naik, Alexis Morvan, Kasra Nowrouzi, Brad Mitchell, David Santiago, and Irfan Siddiqi. 2021. Automatic two-qubit gate calibration with QubiC. *Bull. Amer. Phys. Societ.* (2021).
- [36] Yilun Xu, Gang Huang, David I. Santiago, and Irfan Siddiqi. 2021. Radio frequency mixing modules for superconducting qubit room temperature control systems. *Rev. Sci. Instrum.* 92, 7 (2021), 075108.

Received 21 April 2021; revised 20 January 2022; accepted 28 March 2022